Chemical Science

ROYAL SOCIETY OF CHEMISTRY

EDGE ARTICLE

View Article Online
View Journal | View Issue

Cite this: *Chem. Sci.*, 2026, **17**, 3122

All publication charges for this article have been paid for by the Royal Society of Chemistry

High resolution photoelectron imaging of cryogenically cooled alkaline-earth metal complexes with the BO_2 superhalogen, MBO_2^- (M = Ca, Sr, Ba)

Han-Wen Gao, † Jie Hui, † Xin-Yu Zhang and Lai-Sheng Wang *

The BO_2 molecule is a superhalogen with a very high electron affinity, resulting in an extremely stable BO_2^- anion suitable as a building block to form ionic compounds. Here we report the generation of $M(BO_2^-)$ (M = Ca, Sr, Ba) complexes and the investigation of their structures and bonding using high-resolution cryogenic photoelectron imaging. All three $M(BO_2^-)$ alkaline-earth complexes are found to have linear $M(O–B–O^-)$ ($^1\Sigma^+$) structures. Photodetachment removes an electron from the alkaline-earth metal atom and produces the neutral $M^+(O–B–O^-)$ ($^2\Sigma^+$) ionically bonded ground state. The change of the charge state on the metal center induces a significant reduction of the M–O bond length in the neutral final state, resulting in an extensive M–O stretching vibrational progression in all the photoelectron spectra. The electron affinities of MBO_2 are measured to be 1.574 eV, 1.487 eV, and 1.291 eV and the M–O stretching frequencies are measured to be 411 cm^{-1}, 339 cm^{-1}, and 290 cm^{-1} for M = Ca, Sr, and Ba, respectively. The strong electron-withdrawing power of BO_2 leads to the ionically bonded ground state for MBO_2 ($^2\Sigma^+$), resulting in a single electron localized on the metal center. The ionic interaction between M^+ and BO_2^- in MBO_2 makes their low-lying electronic excitations resemble atomic transitions, rendering MBO_2-type molecules promising candidates for laser cooling.

Received 20th September 2025
Accepted 12th December 2025

DOI: 10.1039/d5sc07306e

rsc.li/chemical-science

1 Introduction

The BO_2 molecule is electron-deficient. Adding an electron to BO_2 gives rise to a very stable BO_2^- anion, which is isoelectronic with CO_2. The electron affinity (EA) of BO_2 was measured by photoelectron spectroscopy (PES) to be 4.46 eV,[1] making it a member of the superhalogen family.[2] The highly stable BO_2^- anion has been used as a building block to design novel ionic complexes and compounds.[3–5] Recently, the alkaline-earth metal complexes with BO_2^-, $M^+(BO_2^-)$, have attracted interest as promising molecular candidates for laser cooling and ultracold chemistry.[6] Laser cooling relies on repeated photon cycling to slow the translational motion of the molecule. Unlike atoms, however, molecules can be lost from the cooling cycle due to vibrational branching. Thus, the key requirement of a laser-coolable molecule is highly diagonal Franck–Condon factors (FCFs).[7–9] The high EA of BO_2 can take one electron away from the alkaline-earth metal M, leaving an isolated M^+ with an unpaired s electron and an $M^+(BO_2^-)$ ionically bonded ground state. Low-lying electronic excitations in MBO_2 involve essentially the atomic transitions of the metal cation M^+, with the BO_2^- ligand being a spectator. To maximize diagonal FCFs, the unpaired electron on M^+ should be as localized as possible, favouring ligands with strong electron-withdrawing power and little covalent interaction with the metal. Recent theoretical calculations show that, among many commonly considered ligands, BO_2 has the highest EA and the strongest electron-withdrawing ability.[6] Thus, the MBO_2 species exhibit the smallest M–O bond length changes upon electronic excitations – the condition to produce diagonal FCFs. However, alkaline-earth MBO_2 complexes have not been studied experimentally and their spectroscopic properties are not known.

On the other hand, there have been extensive studies on the spectroscopy of metal complexes of the isoelectronic CO_2 molecule.[10,11] These complexes are especially interesting as simple models to understand CO_2 activation at the atomic level.[12–26] Negatively charged metal ions, such as Cu^-, Ag^-, Au^-, Ni^-, Pd^-, Pt^-, and Bi^-, can form complexes with CO_2 by attaching to the carbon atom.[13–20] In contrast, positively charged metal ions, such as Mg^+, Ca^+, V^+, and Co^+, bind with CO_2 to form weakly bound, linear $M^+(O–C–O)$ complexes.[21–26] In addition, cyclic structures, in which metals bind simultaneously to both oxygen atoms, have also been observed for neutral alkali metals with CO_2 in low-temperature matrices.[27,28] Despite the rich structures that metal-CO_2 complexes can form, the chemistry of isoelectronic metal-BO_2^- complexes was much less explored.

Department of Chemistry, Brown University, Providence, RI 02912, USA. E-mail: lai-sheng_wang@brown.edu

† These authors contributed equally to this work.

Only a few low-resolution PES studies have been reported on MBO_2^- complexes with M = Cu, Ag, Au, Fe, Al, Na, and Li.[3,29–34]

Motivated by the potential applications of the alkaline-earth metal MBO_2 species in laser cooling and the interest in understanding their structures and bonding, we present a high-resolution photoelectron imaging (PEI) study of MBO_2^- (M = Ca, Sr, Ba). In our PEI experiment, an electron is detached from the MBO_2^- anion, yielding spectroscopic information about the MBO_2 neutral final states. Our high-resolution PEI apparatus was recently equipped with a cryogenic ion trap to create cold cluster anions produced from a laser vaporization source.[35] Cold anions are critical for high-resolution PEI, as demonstrated in recent studies on boron-related clusters.[36–40] In the current work, we have obtained vibrationally resolved photoelectron (PE) spectra for all three MBO_2^- alkaline-earth complexes. Both the anion and the neutral species are shown to be linear. In addition to measuring accurate EAs, we are able to obtain vibrational information for the M–O stretching mode and the B–O stretching modes in the BO_2 moiety. The observation of extensive M–O stretching progression in each case confirms electron detachment from the metal to yield an ionically bonded neutral MBO_2, *i.e.*, $M^+(BO_2^-)$. Experimental and theoretical evidence is presented to show that the atomic nature of M^+ is maintained with BO_2^- being a spectator, which is a key feature of good molecular candidates for laser cooling.

2 Experimental and theoretical methods

2.1 Photoelectron imaging

The experiment was carried out using a high-resolution PEI apparatus recently equipped with a cryogenically cooled 3D Paul trap.[35] Details of the PEI apparatus were described previously.[41] In this study, the MBO_2^- (M = Ca, Sr, Ba) complexes were produced by laser vaporization of cold-pressed M/^{11}B targets, made from the respective metal and ^{11}B-enriched boron powders. Oxygen impurities always existed on the target surface, which could give strong MBO_2^- mass signals especially for fresh targets. To produce stable and consistent MBO_2^- complexes, we employed a helium carrier gas seeded with 0.1% O_2. Clusters formed inside the nozzle were entrained by the carrier gas and underwent a supersonic expansion. After passing through a skimmer, the collimated cluster beam travelled directly into the downstream 3D Paul trap cooled to 4.2 K using a two-stage closed-cycle helium refrigerator. The buffer gas (helium with 20% H_2) was pulsed into the Paul trap on the arrival of the clusters. Negatively charged clusters were trapped and cooled by collisions with the buffer gas. After a 45 ms trapping/cooling time, the cold clusters were extracted into a time-of-flight mass spectrometer. Clusters of interest were mass-selected and intercepted by a detachment laser in the interaction zone of a velocity map imaging system. Photodetachment was performed using the output of a dye laser pumped using a Nd:YAG laser. Photoelectrons were projected onto a microchannel plate coupled with a phosphor screen and the images were recorded using a charge-coupled device camera. The raw images were analysed using the MEVELER method to retrieve the electron kinetic energy distributions.[42] A high resolution of 1.2 cm^{-1} could be achieved for very slow electrons, while for fast electrons, the relative kinetic energy (E_k) resolution ($\Delta E_k/E_k$) was approximately 0.6%.[41]

PEI also yields information about the photoelectron angular distributions (PADs), which are characterized by the anisotropy parameter β. Under the electric dipole approximation, when an electron is ejected from an s atomic orbital with zero angular momentum ($l = 0$), the outgoing electron is a p wave ($l = 1$) with $\beta = 2$. When an electron is ejected from a p atomic orbital ($l = 1$), the outgoing electron carries a mixture of s ($l = 0$) and d ($l = 2$) partial waves with $\beta = -1$.[43] While the β value is non-trivial to interpret for electron detachment from molecular orbitals (MOs), it provides qualitative information about the symmetries of the MOs.[44]

2.2 Theoretical methods

Structure searches were done for the MBO_2^- species using the ABCluster software.[45] For each system, many initial structures were generated and subsequently optimized using density functional theory (DFT) at the PBE0/def2-SVP level[46,47] for both singlet and triplet states. The low-lying isomers were further optimized at the PBE0/def2-TZVP[46,47] level, as presented in Fig. S1. The EAs were computed using the energy differences between the optimized neutral and the anion of the global minimum (GM) structures at the PBE0/def2-TZVP level. Single-point calculations at the CCSD(T)/def2-TZVP level of theory were also performed on the GM structures and the corresponding neutrals to obtain more accurate EAs. Frequency calculations were carried out to compare with the experiment and to ensure that the optimized structures were true minima. All electronic structure calculations were done using the Gaussian 09 package.[48] FCF calculations were performed using the ezFCF package.[49]

3 Experimental and theoretical results

3.1 PEI and PES of $CaBO_2^-$

High-resolution PE images and spectra of $CaBO_2^-$ are measured at 1.599 eV, 1.727 eV, and 1.905 eV, as shown in Fig. 1. The 1.905 eV spectrum (Fig. 1c) reveals extensive vibrational structures. The series of peaks, labelled as 0_0^0, a, b, and d, display similar spacings, which define a vibrational progression. Next to peak d, there is a discernible feature, which is labelled as peak c. Two weak peaks, e and f, are also observed at higher binding energies. The spacing between peaks e and f is similar to the vibrational progression defined by peaks 0_0^0, a, b, and d, suggesting that peak e is due to a high frequency mode and peak f is its combinational level. A weak hot band, labelled as hb, is also observed on the lower binding energy side of the 0_0^0 peak. The hot band yields a vibrational frequency of 331 cm^{-1} for the $CaBO_2^-$ anion. In the 1.727 eV spectrum (Fig. 1b), peaks 0_0^0, a, and b are better resolved. In the 1.599 eV spectrum (Fig. 1a), the 0_0^0 peak, which corresponds to the transition from

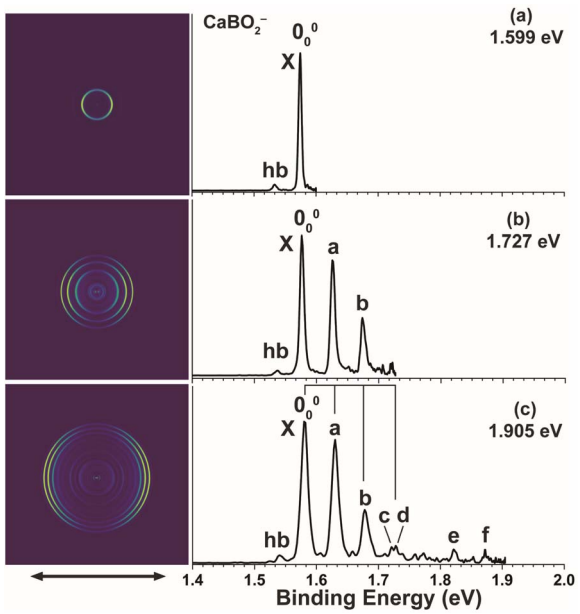

Fig. 1 Photoelectron images and spectra of $CaBO_2^-$ at (a) 1.599 eV, (b) 1.727 eV, and (c) 1.905 eV. The double arrow below the images indicates the laser polarization.

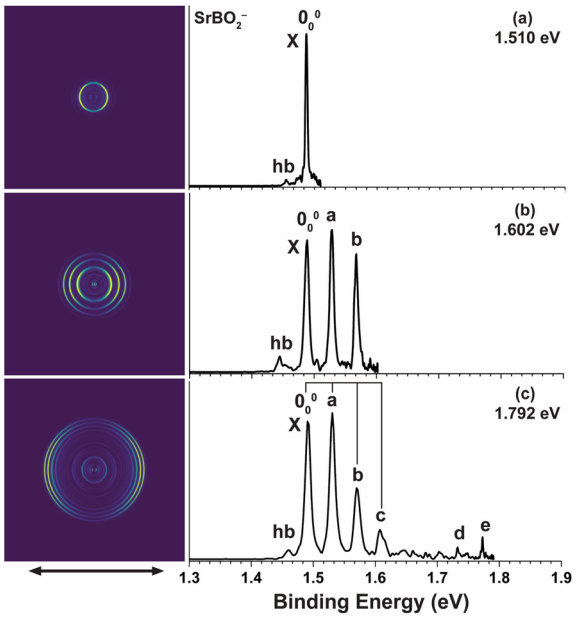

Fig. 2 Photoelectron images and spectra of $SrBO_2^-$ at (a) 1.510 eV, (b) 1.602 eV, and (c) 1.792 eV. The double arrow below the images indicates the laser polarization.

Table 1 The measured binding energies (BEs), assignments, and shifts relative to the 0_0^0 peak for the vibrational features resolved in the spectra of $CaBO_2^-$

	BE (eV)[a]	Assignment	Shift (cm^{-1})	β [b]
hb	1.533(3)	3_1^0	−331	
0_0^0	1.574(1)	$^2\Sigma^+$ (0_0^0)	0	1.7
a	1.625(3)	3_0^1	411	1.6
b	1.675(1)	3_0^2	815	1.3
c	1.722(5)	2_0^1	1194	
d	1.727(5)	3_0^3	1234	
e	1.823(3)	1_0^1	2008	
f	1.872(3)	$1_0^1 3_0^1$	2404	

[a] The numbers in the parentheses represent the uncertainty in the last digit. [b] The β values are obtained from the 1.905 eV spectrum.

the vibrational ground state of the anion to that of the neutral ground state, defines an accurate EA of 1.574 eV for $CaBO_2$. The PADs of all the observed vibrational peaks exhibit distinct p wave characters, implying that the detached electron originates from an s or σ-type orbital. Note that the β values depend on the electron kinetic energies (Table 1). The β value of 1.7 for the 0_0^0 transition is very close to the ideal value of 2 for electron detachment from atomic s orbitals, indicating the near atomic-like highest occupied molecular orbital (HOMO) of $CaBO_2^-$, from which an electron is removed in the PEI experiment. The binding energies of all the vibrational peaks, their shifts relative to peak 0_0^0, their assignments, and β values are given in Table 1.

3.2 PEI and PES of $SrBO_2^-$

High-resolution PE images and spectra of $SrBO_2^-$ measured at 1.510 eV, 1.602 eV, and 1.792 eV are presented in Fig. 2. The 1.792 eV spectrum (Fig. 2c) exhibits a vibrational progression closely resembling that for $CaBO_2^-$. The main progression is represented by peaks 0_0^0, a, b, and c, with similar spacings. Similarly, peak d suggests a high frequency mode and peak e indicates its combinational level. A vibrational hot band (labelled hb) is also observed, giving a vibrational frequency of 258 cm^{-1} for the anion. The 1.602 eV spectrum (Fig. 2b) resolves peaks 0_0^0, a, and b better and the 1.510 eV spectrum (Fig. 2a) defines an accurate EA of 1.487 eV for $SrBO_2$. All observed vibrational peaks exhibit distinct p wave angular distributions with the β values close to 2 for atomic s orbitals, similar to that in $CaBO_2^-$, suggesting electron detachment from an s or σ-type orbital. The binding energies of all the observed peaks, their shifts relative to peak 0_0^0, their assignments, and β values are given in Table 2.

Table 2 The measured binding energies (BEs), assignments, and shifts relative to the 0_0^0 peak for the vibrational features resolved in the spectra of $SrBO_2^-$

	BE (eV)[a]	Assignment	Shift (cm^{-1})	β [b]
hb	1.455(3)	3_1^0	−258	
0_0^0	1.487(1)	$^2\Sigma^+$ (0_0^0)	0	1.6
a	1.529(3)	3_0^1	339	1.6
b	1.568(1)	3_0^2	653	1.3
c	1.611(5)	$3_0^3/2_0^1$	1000	
d	1.734(3)	1_0^1	1992	
e	1.774(3)	$1_0^1 3_0^1$	2315	

[a] The numbers in the parentheses represent the uncertainty in the last digit. [b] The β values are obtained from the 1.792 eV spectrum.

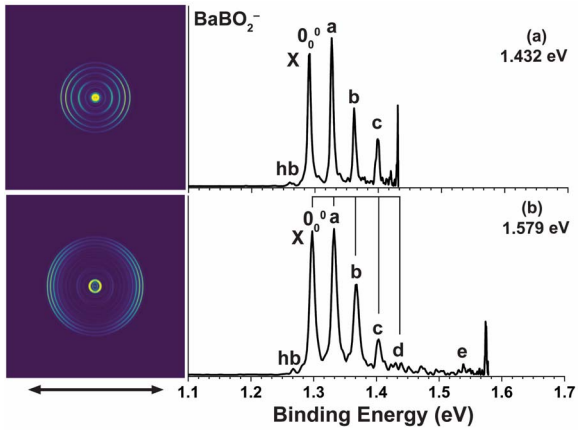

Fig. 3 Photoelectron images and spectra of $BaBO_2^-$ at (a) 1.432 eV and (b) 1.579 eV. The double arrow below the images indicates the laser polarization.

Table 3 The measured binding energies (BEs), assignments, and shifts relative to the 0_0^0 peak for the vibrational features resolved in the spectra of $BaBO_2^-$

	BE (eV)[a]	Assignment	Shift (cm^{-1})	β [b]
hb	1.261(3)	3_1^0	−242	
0_0^0	1.291(3)	$^2\Sigma^+$ (0_0^0)	0	1.6
a	1.327(3)	3_0^1	290	1.5
b	1.362(3)	3_0^2	573	1.4
c	1.399(3)	3_0^3	871	
d	1.436(5)	3_0^4	1170	
e	1.540(5)	1_0^1	2008	

[a] The numbers in the parentheses represent the uncertainty in the last digit. [b] The β values are obtained from the 1.579 eV spectrum (Fig. 3b).

3.3 PEI and PES of $BaBO_2^-$

High-resolution PE images and spectra of $BaBO_2^-$ at 1.432 eV and 1.579 eV are presented in Fig. 3. An extensive vibrational progression is revealed, similar to those of $CaBO_2^-$ and $SrBO_2^-$. The main progression is represented by peaks 0_0^0, a, b, c, and d with nearly equal spacing. The 0_0^0 transition defines an EA of 1.291 eV for $BaBO_2$. The weak hot band (labelled hb) gives an anion vibrational frequency of 242 cm^{-1}. All observed vibrational peaks also exhibit distinct p wave angular distributions with β values close to 2 for s atomic orbitals, similar to those of $CaBO_2^-$ and $SrBO_2^-$, indicating detachment from an s or σ-type orbital. The two PE spectra for $BaBO_2^-$ in Fig. 3 each show a sharp threshold peak, probably due to threshold enhancement of part of a threshold vibronic transition, possibly involving the sequence bands of the hot band transitions. The binding energies of the observed vibrational peaks, their shifts relative to peak 0_0^0, their assignments, and β values are given in Table 3.

3.4 Theoretical results

Structure searches (Fig. S1) find that the closed-shell linear M–O–B–O^- structure with $C_{\infty v}$ symmetry ($^1\Sigma^+$) is overwhelmingly

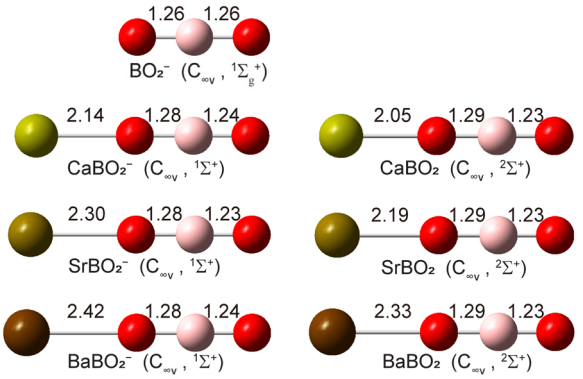

Fig. 4 The optimized structures of $CaBO_2^-$, $SrBO_2^-$, $BaBO_2^-$ and their neutrals at the PBE0/def2-TZVP level. The optimized structure of BO_2^- is also shown for comparison. The point group symmetries and electronic states are also given. The bond lengths are given in Å.

Table 4 The experimental EAs and vibrational frequencies compared with the calculated values for MBO_2 (M = Ca, Sr, Ba)

	EA (eV)		Frequency (cm^{-1})[a]	
	Exp.	Cal.[b]	Exp.[c]	Cal.
$CaBO_2$	1.574	1.52	411 (ν_3)	372
			1193 (ν_2)	1105
			2008 (ν_1)	1978
$SrBO_2$	1.487	1.45	339 (ν_3)	300
			992 (ν_2)	1093
			1992 (ν_1)	1990
$BaBO_2$	1.291	1.23	290 (ν_3)	275
			2008 (ν_1)	1998

[a] Calculated frequencies at the PBE0/def2-TZVP level are scaled by a factor of 0.96. The vibrational displacement vectors are shown in Fig. S2. [b] At the CCSD(T)/def2-TZVP level. The EAs computed at the PBE0/def2-TZVP level are 1.48, 1.35, and 1.22 eV for M = Ca, Sr, and Ba, respectively. [c] The experimental uncertainty is estimated to be ±10 cm^{-1}.

the global minimum for all MBO_2^- species, as shown in Fig. 4. The B–O bond lengths are all similar to those in bare BO_2^- (shown in Fig. 4 for comparison): the B–O bond close to the metal is slightly elongated while the B–O bond away from the metal is slightly shortened. The molecular orbitals (MOs) for MBO_2^- are given in Fig. S2. The HOMO of MBO_2^- is essentially the valence s orbital on the metal atom, polarized only slightly by the BO_2^- ligand. Removing an electron from the HOMO gives rise to the doublet $^2\Sigma^+$ ground state of neutral MBO_2 (Fig. 4). The B–O bond lengths remain almost the same in the neutral as in the anion, but the M–O bond length is significantly shortened, which should induce a large vibrational progression in the PE spectra in the M–O stretching mode. The calculated EAs for MBO_2 (M = Ca, Sr, Ba), using single-point energies calculated at the CCSD(T)/def2-TZVP level for the linear GM structures, are compared with the corresponding experimental values in Table 4. The calculated vibrational frequencies for the stretching modes of neutral MBO_2, scaled by a factor of 0.96,[50] are also compared with the experimental data in Table 4.

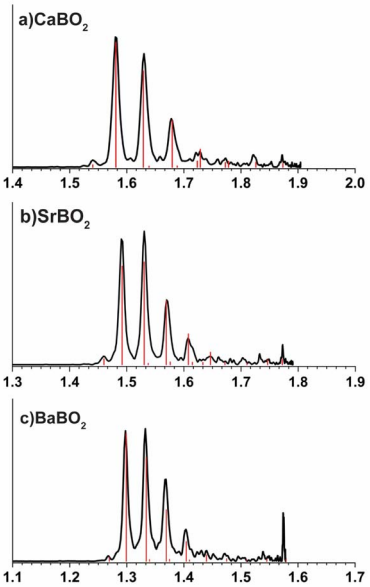

Fig. 5 Calculated Franck–Condon factors for the ground state detachment transitions of (a) $CaBO_2^-$, (b) $SrBO_2^-$, and (c) $BaBO_2^-$.

4 Discussion

4.1 Comparison between experiment and theory

The calculated EAs for the linear GM structures of $CaBO_2$, $SrBO_2$, and $BaBO_2$ at the CCSD(T)/def2-TZVP level are 1.52 eV, 1.45 eV, and 1.23 eV, and they are in excellent agreement with the experimental data of 1.547 eV, 1.487 eV and 1.291 eV, respectively, as shown in Table 4. To understand the observed vibrational structures, we computed the FCFs using the optimized geometries and vibrational frequencies of the anions and neutrals at the PBE0/def2-TZVP level, as shown in Fig. 5. The most FC-active mode is the M–O stretching (ν_3 in Fig. S3), as expected. The calculated FCFs are in excellent agreement with the PE spectra, allowing all the vibrational features to be readily assigned.

The extensive ν_3 vibrational progression in all three systems agrees with the large change in the M–O bond length upon electron detachment. The observed hot band in each spectrum comes from the FC-active M–O stretching mode of the anions, measured to be 331 cm^{-1}, 258 cm^{-1}, and 242 cm^{-1} for $CaBO_2^-$, $SrBO_2^-$, and $BaBO_2^-$, respectively. The M–O stretching frequencies in the anions are all much smaller than those in the neutrals (Table 4), as expected. The FCF calculations suggest a vibrational temperature of ~100 K, which is higher than we expected, probably due to gas condensation in the interior of the ion trap. The presence of the weak hot band, nonetheless, did not affect the resolution of the PE spectra, but allowed the anion vibrational frequencies to be measured.

The computed FCFs suggest that peak c in the $CaBO_2^-$ spectrum can be assigned to the ν_2 mode, that is, the symmetric stretching of the O–B–O moiety (Fig. S3); peak e is due to the ν_1 mode, which is the asymmetric stretching of the O–B–O moiety (Fig. S3), while peak f is the combinational level between ν_1 and ν_3. Similarly, in the $SrBO_2^-$ spectrum, peak d can be assigned to the ν_1 mode and peak e is due to the combinational level between ν_1 and ν_3. In the $BaBO_2^-$ spectrum, peak e can be assigned to the ν_1 mode. There are only three linear stretching modes for the linear M–O–B–O molecules. We are able to observe all of them for $CaBO_2$. The weak FC activities for the ν_1 and ν_2 modes are due to the very small B–O bond length changes from the anion to the neutral (Fig. 4). Note that the asymmetric O–B–O stretching frequency and symmetric O–B–O stretching frequency in bare BO_2^- are 1992 cm^{-1} and 1110 cm^{-1}, respectively, which are similar to those observed in $CaBO_2$. For $SrBO_2$, we are only able to resolve the ν_1 transition; the ν_2 vibration is very close to the 3_0^3 transition (peak c, Fig. 2c). In the case of $BaBO_2$, the ν_2 vibrational frequency is very close to the 3_0^4 transition (peak d, Fig. 3b). Overall, the excellent agreement of the calculated EAs and the calculated FCFs with the experimental data unequivocally confirms the linear structures for both the MBO_2^- anion and MBO_2 neutral species.

4.2 Chemical bond analyses

The computed structures (Fig. 4) and the experimental vibrational information all indicate that the BO_2^- anion moiety remains intact in both the MBO_2^- anion and the MBO_2 neutral. In addition to the atomic-like σ HOMO, we find that the remaining valence MOs of the BO_2^- moiety in MBO_2^- are similar to those of the bare BO_2^- anion, as shown in Fig. S2. Natural charge analyses were carried out for $CaBO_2^-$, $SrBO_2^-$, and $BaBO_2^-$ and their neutrals, as shown in Fig. 6. In the MBO_2^- anions, the metal atom is essentially neutral, carrying negligible charges, whereas the BO_2 moiety retains the unit negative charge. The intact nature of BO_2^- is further supported by the similarity of the B–O bond lengths in MBO_2^- and MBO_2 compared with those in bare BO_2^- (Fig. 4).

Thus, the MBO_2^- anion is essentially a neutral alkaline-earth atom interacting weakly with the BO_2^- anion. The negative charge on the ligand polarizes the spherically symmetric valence s electron cloud, inducing a dipole moment on the metal and giving rise to a dipole–charge interaction. This polarization interaction distorts the charge distribution on BO_2^- with more negative charge pulled to the oxygen atom bound to the metal. The induced-dipole–charge interaction is the reason why the linear M–O–B–O^- geometry is favoured.

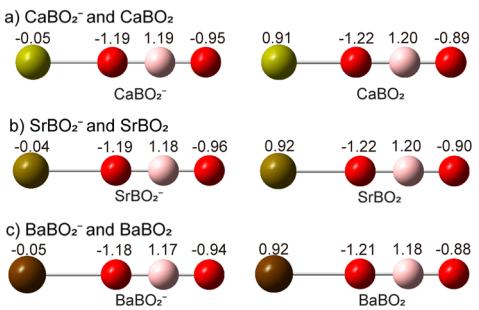

Fig. 6 Natural charge distributions for (a) $CaBO_2^-$ and $CaBO_2$, (b) $SrBO_2^-$ and $SrBO_2$, and (c) $BaBO_2^-$ and $BaBO_2$.

Photodetachment from the HOMO of the MBO_2^- anion, which is essentially the metal valence s orbital, leads to the $^2\Sigma^+$ neutral ground state, leaving one s electron localized on the alkaline-earth metal cation. Natural charge analyses indicate that, in the neutral MBO_2 complexes, the metal carries nearly a unit positive charge (Fig. 6 and Table S1), while the BO_2^- ligand retains its unit negative charge. Thus, neutral MBO_2 is a completely ionic molecule between M^+ and BO_2^-, leading to the significantly shortened M–O bond length compared to that in the anion due to the strong Coulombic interaction. This large bond-length contraction gives rise to the pronounced M–O stretching progressions in the PE spectra. We analysed the spin densities of MBO_2, showing that the unpaired spin is nearly completely localized on the metal (Table S1). The ionic bonding nature between M^+ and BO_2^- in MBO_2 is further supported by the Wiberg bond indices (Table S2), which indicate negligible covalent bonding between the M^+ and BO_2^- fragments. It is interesting to note that ionization of the valence s electron from M in $M(BO_2^-)$ requires much less energy in comparison to the ionization energies of the bare metal atoms (6.11 eV for Ca, 5.69 eV for Sr, and 5.21 eV for Ba) due to the Coulombic repulsion from the negatively charged BO_2^- ligand.

4.3 Implications for laser cooling

The alkaline-earth MBO_2 complexes are promising laser cooling candidates because of the superhalogen property of BO_2 that results in an ionic $M^+(BO_2^-)$ species and leaves a single isolated s electron on the alkaline-earth metal cation M^+. Thus, the cycling transition happens on the metal centre with highly diagonal FCFs while the BO_2^- ligand is a spectator. Note that the current PEI experiments do not directly probe the MBO_2 excited states within the cycling transition; the extensive FCFs observed in the current study correspond to photodetachment transitions from the MBO_2^- anion to neutral MBO_2. Nevertheless, the PEI experiment provides valuable information about the structures and vibrational frequencies of the MBO_2 neutral ground state and the nature of the atomic-like HOMO on the metal site. The observed large M–O stretching progression confirms the cationic nature of M^+ and its dominating ionic interaction with BO_2^-. The angular distributions of the PE images and the β values show that the photodetachment transition comes from a nearly ideal s orbital on the metal site, because of the electrostatic nature of the metal–ligand interactions in both MBO_2^- and MBO_2. It is expected that the electrostatic interaction in $M^+(BO_2^-)$ would not be affected significantly upon the s to p cycling transition, making the MBO_2 systems excellent laser cooling targets. Indeed, recent theoretical calculations predict that the alkaline-earth MBO_2 complexes exhibit very small M–O bond length changes upon s to p excitation,[6] conducive to yielding highly diagonal FCFs. Additionally, the current study shows that the MBO_2 complexes can be readily generated in a laser vaporization cluster source. The number density of the neutral MBO_2 species from the laser vaporization source is expected to be much higher than that of the MBO_2^- anions used for the current PEI experiments.

5 Conclusion

In conclusion, we report an investigation of $CaBO_2^-$, $SrBO_2^-$ and $BaBO_2^-$ and their corresponding neutrals (MBO_2) using high-resolution photoelectron imaging. The electron affinities of neutral $CaBO_2$, $SrBO_2$, and $BaBO_2$ are measured to be 1.574 eV, 1.487 eV and 1.291 eV, respectively. Vibrationally resolved photoelectron imaging, combined with computational chemistry, confirms that the MBO_2^- anions have linear M–O–B–O^- structures with a singlet $^1\Sigma^+$ ground state and the MBO_2 neutrals all have ionically bonded linear $M^+[O–B–O]^-$ structures with a doublet ($^2\Sigma^+$) ground state. Chemical bond analyses show that the MBO_2^- anion consists of essentially a neutral alkaline-earth atom weakly interacting with a BO_2^- ligand. Photodetachment removes an electron from the metal atom, resulting in the $M^+(BO_2^-)$ ionic compound for neutral MBO_2. The M–O stretching vibrational frequencies for all three MBO_2 complexes are measured, and in the case of $CaBO_2$, both the B–O symmetric and asymmetric stretching frequencies are also measured. The atomic nature of the HOMO in MBO_2 is also revealed from the angular distributions of the photoelectron images. The current study confirms the recent theoretical study that suggests that alkaline-earth MBO_2 complexes are ideal molecular systems for laser cooling.

Author contributions

J. H. led the experiment. H. W. G. and X. Y. Z. helped with the experiment. J. H. did the calculations. H. W. G. and J. H. analysed the data. H. W. G. led the writing of the manuscript. L. S. W. guided and advised the project and revised and finalized the manuscript.

Conflicts of interest

There are no conflicts to declare.

Data availability

The data that supports the findings of this study is available from the corresponding author upon request.

Supplementary information (SI) is available. See DOI: https://doi.org/10.1039/d5sc07306e.

Acknowledgements

This work was supported by the U.S. National Science Foundation (Grant No. CHE-2403841). The calculations were performed using resources at the Centre for Computation and Visualization (CCV) of Brown University.

References

1 H. J. Zhai, L. M. Wang, S. D. Li and L. S. Wang, *J. Phys. Chem. A*, 2007, **111**, 1030.
2 G. L. Gutsev and A. I. Boldyrev, *Chem. Phys.*, 1981, **56**, 277.

3 M. Willis, M. Götz, A. K. Kandalam, G. F. Ganteför and P. Jena, *Angew. Chem., Int. Ed.*, 2010, **49**, 8966.
4 C. Huang, M. Mutailipu, F. Zhang, K. J. Griffith, C. Hu, Z. Yang, J. M. Griffin, K. R. Poeppelmeier and S. Pan, *Nat. Commun.*, 2021, **12**, 2597.
5 S. Liu, X. Jiang, L. Qi, Y. Hu, K. Duanmu, C. Wu, Z. Lin, Z. Huang, M. G. Humphrey and C. Zhang, *Angew. Chem., Int. Ed.*, 2024, **63**, e202403328.
6 M. V. Ivanov, F. H. Bangerter and A. I. Krylov, *Phys. Chem. Chem. Phys.*, 2019, **21**, 19447.
7 M. D. Rosa, *Eur. Phys. J. D*, 2004, **31**, 395.
8 T. A. Isaev and R. Berger, *Phys. Rev. Lett.*, 2016, **116**, 063006.
9 S. Vadachkoria, Q. Lei, T. C. Steimle and M. C. Heaven, *J. Phys. Chem. Lett.*, 2025, **16**, 3309.
10 M. A. Duncan, *Int. Rev. Phys. Chem.*, 2003, **22**, 407.
11 N. C. Polfer and J. Oomens, *Mass Spectrom. Rev.*, 2009, **28**, 468.
12 D. K. Böhme and H. Schwarz, *Angew. Chem., Int. Ed.*, 2005, **44**, 2336.
13 A. D. Boese, H. Schneider, A. N. Glöß and J. M. Weber, *J. Chem. Phys.*, 2005, **122**, 154301.
14 B. J. Knurr and J. M. Weber, *J. Am. Chem. Soc.*, 2012, **134**, 18804.
15 B. J. Knurr and J. M. Weber, *J. Phys. Chem. A*, 2013, **117**, 10764.
16 B. J. Knurr and J. M. Weber, *J. Phys. Chem. A*, 2014, **118**, 10246.
17 X. Zhang, E. Lim, S. K. Kim and K. H. Bowen, *J. Chem. Phys.*, 2015, **143**, 174305.
18 M. C. Thompson, J. Ramsay and J. M. Weber, *Angew. Chem., Int. Ed.*, 2016, **55**, 15171.
19 G. Liu, S. M. Ciborowski, Z. Zhu, Y. Chen, X. Zhang and K. H. Bowen, *Phys. Chem. Chem. Phys.*, 2019, **21**, 10955.
20 R. Wang, G. Liu, S. K. Kim, K. H. Bowen and X. Zhang, *J. Energy Chem.*, 2021, **63**, 130.
21 M. Sodupe, C. W. Bauschlicher and H. Partridge, *Chem. Phys. Lett.*, 1992, **192**, 185.
22 C. S. Yeh, K. F. Willey, D. L. Robbins, J. S. Pilgrim and M. A. Duncan, *J. Chem. Phys.*, 1993, **98**, 1867.
23 C. T. Scurlock, S. H. Pullins and M. A. Duncan, *J. Chem. Phys.*, 1996, **105**, 3579.
24 G. Gregoire, J. Velasquez and M. A. Duncan, *Chem. Phys. Lett.*, 2001, **349**, 451.
25 N. R. Walker, G. A. Grieves, R. S. Walters and M. A. Duncan, *Chem. Phys. Lett.*, 2003, **380**, 230.
26 N. R. Walker, R. S. Walters and M. A. Duncan, *J. Chem. Phys.*, 2004, **120**, 10037.
27 Z. H. Kafafi, R. H. Hauge, W. E. Billups and J. L. Margrave, *Inorg. Chem.*, 1984, **23**, 177.
28 V. N. Solov'ev, E. V. Polikarpov, A. V. Nemukhin and G. B. Sergeev, *J. Phys. Chem. A*, 1999, **103**, 6721.
29 Y. Feng, H. G. Xu, Z. G. Zhang, Z. Gao and W. Zheng, *J. Chem. Phys.*, 2010, **132**, 074308.
30 Y. Feng, H. G. Xu, W. Zheng, H. Zhao, A. K. Kandalam and P. Jena, *J. Chem. Phys.*, 2011, **134**, 094309.
31 X. Y. Kong, H. G. Xu, P. Koirala, W. J. Zheng, A. K. Kandalam and P. Jena, *Phys. Chem. Chem. Phys.*, 2014, **16**, 26067.
32 G. L. Gutsev, C. A. Weatherford, L. E. Johnson and P. Jena, *J. Comput. Chem.*, 2012, **33**, 416.
33 Y. Feng, M. Cheng, X. Y. Kong, H. G. Xu and W. J. Zheng, *Phys. Chem. Chem. Phys.*, 2011, **13**, 15865.
34 Z. Zeng, G. L. Hou, J. Song, G. Feng, H. G. Xu and W. J. Zheng, *Phys. Chem. Chem. Phys.*, 2015, **17**, 9135.
35 G. S. Kocheril, H. W. Gao, D. F. Yuan and L. S. Wang, *J. Chem. Phys.*, 2022, **157**, 171101.
36 H. W. Gao, H. W. Choi, J. Hui, W. J. Chen, G. S. Kocheril and L. S. Wang, *J. Chem. Phys.*, 2023, **159**, 114301.
37 H. W. Gao, H. W. Choi, J. Hui and L. S. Wang, *J. Phys. Chem. A*, 2024, **128**, 3579.
38 H. W. Gao, J. Hui and L. S. Wang, *Chem. Commun.*, 2023, **59**, 12431.
39 H. W. Gao, J. Hui and L. S. Wang, *J. Phys. Chem. Lett.*, 2025, **16**, 2039.
40 H. W. Gao, J. Hui and L. S. Wang, *Chem. Sci.*, 2025, **16**, 7004.
41 I. León, Z. Yang, H. T. Liu and L. S. Wang, *Rev. Sci. Instrum.*, 2014, **85**, 083106.
42 B. Dick, *Phys. Chem. Chem. Phys.*, 2019, **21**, 19499.
43 J. Cooper and R. N. Zare, *J. Chem. Phys.*, 1968, **48**, 942.
44 A. Sanov and R. Mabbs, *Int. Rev. Phys. Chem.*, 2008, **27**, 53.
45 J. Zhang and M. Dolg, *Phys. Chem. Chem. Phys.*, 2015, **17**, 24173.
46 C. Adamo and V. Barone, *J. Chem. Phys.*, 1999, **110**, 6158.
47 F. Weigend and R. Ahlrichs, *Phys. Chem. Chem. Phys.*, 2005, **7**, 3297.
48 M. J. Frisch *et al.*, *Gaussian 09, Revision A.1*, Gaussian, Inc., Wallingford, CT, 2009.
49 S. Gozem and A. I. Krylov, *WIREs Comp. Mol. Sci.*, 2021, **12**, e1546.
50 NIST computational chemistry comparison and benchmark database, https://cccbdb.nist.gov/vibscalejustx.asp.